High-resolution multifluid simulations of flux ropes in the Martian magnetosphere

E. M. Harnett[1]

Received 29 July 2008; revised 13 October 2008; accepted 13 November 2008; published 16 January 2009.

[1] Three-dimensional multifluid simulations of the Martian magnetosphere show the development and dynamics of flux ropes. One flux rope, which is analyzed in detail, initiates at a reconnection region near the dusk terminator and travels tailward with a speed on the order of 40 km s^{-1}. The reconnection region forms close to the planet at an altitude of 700 km. Both the location of the reconnection and energy spectra of the plasma in the reconnection region agree with Mars Global Surveyor observations of reconnection. The largest flux ropes have a spatial extent on the order of 2000 km. Energy spectra taken through the flux ropes show an inverted-V type structure similar to those measured by Mars Express, suggesting that some inverted-V observations may be transits through flux ropes. The simulations indicate that the formation of flux ropes can lead to enhanced loss of heavy ions from the atmosphere.

Citation: Harnett, E. M. (2009), High-resolution multifluid simulations of flux ropes in the Martian magnetosphere, *J. Geophys. Res.*, *114*, A01208, doi:10.1029/2008JA013648.

1. Introduction

[2] Fifty years of space-based observations around the Earth have yielded a wealth of knowledge about the terrestrial magnetosphere. But for all we have learned, it is still only a single case study. Mars represents a different end member from the Earth with regard to the study of magnetospheres. Similar to the Earth, a bow shock and magnetosheath form around Mars, but owing to the lack of global magnetic field, the bow shock forms close to the planet, with an average stand-off distance of 1.64 R_M [*Vignes et al.*, 2000]. Instead of a magnetopause, a magnetic pileup boundary (MPB) forms at the inner edge of the magnetosheath where the interplanetary magnetic field (IMF) begins to pile up around the planet, forming the magnetic pileup region (MPR). The MPR forms the boundary between solar wind dominated plasma and plasma of planetary origin [e.g., *Betucci et al.*, 2005; *Brain*, 2006]. The average stand-off distance of the MPB is 1.29 R_M [*Vignes et al.*, 2000]. At the inner edge of the MPR forms the photoelectron boundary (PEB). The PEB is the upper edge of the planetary ionosphere and has a mean altitude of 430 km [*Mitchell et al.*, 2001]. Complicating this picture is the presence of crustal magnetic fields [*Acuna et al.*, 1998, 1999]. These magnetic anomalies modify the local plasma environment, increasing the altitude of the MPB [*Crider et al.*, 2002; *Brain et al.*, 2005] and the PEB [*Mitchell et al.*, 2001], protecting the upper atmosphere from incident electrons [*Brain et al.*, 2007]. Thus most of the solar wind interaction at Mars occurs close to the planet, in contact with the ionosphere and atmosphere. This is different from the solar wind interaction with the Earth, where the majority of the interaction occurs far from the surface.

[3] One similarity between the Earth and Mars is the observation of inverted-V particle spectra. Inverted-V ion and electron spectra have been observed many times by Mars Express (MEX) [*Lundin et al.*, 2006a, 2006b]. Inverted-V spectra are commonly observed at the boundary between open and closed magnetic field lines in the Earth's auroral region, and are associated with potential drops along the magnetic field [e.g., *Lin and Hoffman*, 1982]. *Lundin et al.* [2006a] found that the inverted-V spectra at Mars are typically observed at the boundary separating regions of always closed magnetic field and always radial magnetic field, as determined by Mars Global Surveyor (MGS) observations at 400 km. At the same time inverted-Vs are measured, MEX typically observes an upward flux of ionospheric ions and a downward flux of electrons. This combination of data has lead to the interpretation that the observation of inverted-Vs at Mars are an indication of parallel electric fields and auroral-type structures.

[4] *Lundin et al.* [2006a] determined that the nature of the spectra suggests that the acceleration processes are variable but driven by solar wind conditions. Analysis of additional times when inverted-V spectra were observed [*Lundin et al.*, 2006b] showed an uneven split in the beam energy and beam temperature indicating acceleration processes that are both parallel and perpendicular to the magnetic field. *Lundin et al.* [2006b] determined that acceleration occurred through a combination of pondermotive forcing (possibly induced by Alfven or ion cyclotron waves) and electrostatic acceleration, with electrostatic acceleration providing between one-half and two-thirds of the acceleration.

[5] Electron acceleration and field-aligned currents were also observed by MGS [*Brain et al.*, 2006]. Thousands of aurora-like electron spectra have been seen with peak energies between 100–500 eV and a flux an order of magnitude

[1]Department of Earth and Space Sciences, University of Washington, Seattle, Washington, USA.

0148-0227/09/2008JA013648

larger than the flux in surrounding areas. Statistical analysis suggests the origin of these aurora-like plasma populations is due to reconnection of the anomalous magnetic field with the interplanetary magnetic field (IMF), with such spectra preferentially seen during intervals of low solar wind dynamic pressure in the northern hemisphere summer [*Brain et al.*, 2006]. *Eastwood et al.* [2008] (and private communication, 2008) found direct evidence in MGS data for reconnection in thin current sheets, including bifurcations of the current sheet. They also found multiple cases of a bipolar signature in the magnetic field component normal to the observed current sheet, consistent with the formation of magnetic islands. In the reconnection regions, Hall magnetic field structures were observed, most likely associated with differential ion and electron motion.

[6] While the MGS and MEX observations complement each other the picture is not complete. The combination of observations of high-energy electron populations and a reconnection-like magnetic field geometry by MGS at an altitude of 400 km [*Brain et al.*, 2006] suggests an acceleration region close to the planet. *Lundin et al.* [2006b] determined that most of the acceleration occurs in a region below 2000 km but several of the observations of inverted-Vs by MEX are at altitudes in excess of 4000 km and the low-altitude inverted-V ($\sim$1000 km) showed no indication of ion acceleration suggesting a more extended acceleration region. *Brain et al.* [2006] suggested that reconnection near the planet, somehow modulated by the solar wind conditions, is the source of electron acceleration seen in MGS observations. Conversely, *Lundin et al.* [2006b] propose a solar wind driven dynamo processes occurring down tail for driving the observed field-aligned currents. While auroral-like UV emissions have been observed at Mars [*Bertaux et al.*, 2005], it is not clear how the observations of auroral-like particle spectra both near and far from the planet relate to the processes that lead to aurora.

[7] This paper presents results from 3-D multifluid simulations of the Martian magnetosphere for high-speed solar wind conditions. While changes in the solar wind speed lead to multiple changes in the Martian magnetosphere, this paper focuses on the formation of flux ropes. One flux rope, which forms near the dusk side terminator as the result of reconnection, is analyzed in detail. An additional case is analyzed as it exhibits different propagation characteristics. The simulation results in the vicinity of the flux ropes, a reconnection region, and a region in the vicinity of an open-closed magnetic field line boundary are compared to observations by MEX and MGS, focusing particularly on the observations of inverted-V spectra.

2. Model

[8] The multifluid model [*Winglee*, 2004] has been used to investigate flux ropes at the magnetopause of the terrestrial magnetosphere [*Winglee et al.*, 2008a], thin current sheets in the terrestrial magnetotail [*Harnett et al.*, 2006], and to study weakly magnetized systems, e.g., Pluto [*Harnett et al.*, 2005] and Ganymede [*Paty and Winglee*, 2006]. The simulation simultaneously tracks multiple, separate ion fluids and an electron fluid. The inclusion of mass effects, using a modified Ohm's law and ion cyclotron effects in the full conservation of momentum equation, allows us to track the manner in which different ions are accelerated. This type of model is well suited to the study of flux ropes within a global magnetosphere. Like hybrid and full particle models, the multifluid technique can capture ion cyclotron effects which are crucial in the development of flux ropes. This physics is missing from ideal MHD models. Hybrid and particle codes have the advantage that they can predict non-Maxwellian distributions, thus multifluid models will typically underestimate the energization of plasma in regions where wave-particle interactions are significant. But the multifluid model has the advantage that it can simulate global systems, such as an entire magnetosphere, with locally high resolution. This feature is essential for resolving thin current sheets in which reconnection can occur, producing flux ropes. Hybrid simulations can produce either global coverage [e.g., *Brecht*, 1997] or simulate only a small region with high resolution [e.g., *Drake et al.*, 2003]. And the computational resources required for particle simulations are such that only small regions are simulated [e.g., *Eastwood et al.*, 2008].

[9] The multifluid model solves the following equations using a dynamically determined time step:

$$\frac{\partial \rho_i}{\partial t} + \nabla \cdot (\rho_i \vec{v}_i) = 0 \tag{1}$$

$$\rho_i \frac{d\vec{v}_i}{dt} = n_i q_i \left(\vec{E} + \vec{v}_i \times \vec{B}\right) - \nabla P_i - \left(\frac{GM_M}{R^2}\right)\rho_i \vec{r} \tag{2}$$

$$\frac{\partial P_i}{\partial t} = -\gamma \nabla \cdot (P_i \vec{v}_i) + (\gamma - 1)\vec{v}_i \cdot \nabla P_i \tag{3}$$

The subscript i denotes an individual ion population. The terms in the equations are ρ_i is the mass density, v_i the bulk velocity, n_i the number density, and q_i the charge. G is the gravitational constant, M_M the mass of Mars, $\vec{E}$ the electric field, $\vec{B}$ the magnetic field. P_i is the pressure for each ion species i and γ is the ratio of specific heats (5/3).

[10] The electron dynamics are determined by a pressure equation

$$\frac{\partial P_e}{\partial t} = -\gamma \nabla \cdot (P_e \vec{v}_{de}) + (\gamma - 1)\vec{v}_{de} \cdot \nabla P_e \tag{4}$$

where the electrons are assumed to have sufficiently high mobility along the magnetic field such that they are approximately in steady state (i.e., $dv_{de}/dt = 0$) or in drift motion. The electron drift velocity is equal to

$$\vec{v}_{de} = \sum_i \frac{n_i}{n_e}\vec{v}_i - \frac{\vec{J}}{en_e} \tag{5}$$

and quasi-neutrality is assumed

$$n_e = \sum_i n_i \tag{6}$$

[11] The equations are closed with

$$\frac{\partial \vec{B}}{\partial t} = -\nabla \times \vec{E} \tag{7}$$

$$\vec{J} = \frac{1}{\mu_o}\nabla \times \vec{B} \tag{8}$$

and by assuming a modified Ohm's law:

$$\vec{E} = -\sum_i \frac{n_i}{n_e}\vec{v}_i \times \vec{B} + \frac{\vec{J}\times\vec{B}}{en_e} - \frac{\nabla P_e}{en_e} + \eta(\vec{r})\vec{J} \quad (9)$$

where n_e is the electron number density, e the electron charge, $\vec{J}$ the current density, and η is the resistivity, added to allow finite conductivity only in the ionosphere. The resistivity is zero at all other locations, thus there is no anomalous resistivity in our model. The Hall and pressure gradient terms in Ohm's law (9) are sufficient to drive reconnection. The pressure gradient term is also responsible for generating parallel electric fields. Numerical resistivity is also not an issue with regard to driving reconnection. Previous simulations of the terrestrial current sheet [*Harnett et al.*, 2006] have shown that provided the resolution is high enough to resolve given structures (such as the spatial variability of ions and electrons within a thin current sheet), the results are independent of grid resolution. Thus increasing grid resolution (and changing the numerical resistivity) does not change the results.

[12] On substituting (9) into the momentum equation (2) we obtain

$$\rho_i \frac{d\vec{v}_i}{dt} = q_i n_i \left(\vec{v}_i - \sum_i \frac{n_i}{n_e}\vec{v}_i\right) \times \vec{B} + \frac{q_i n_i}{en_e}\left(\vec{J}\times\vec{B} - \nabla P_e\right) - \nabla P_i + q_i n_i \eta \vec{J} - \left(\frac{GM_M}{R^2}\right)\rho_i \vec{r} \quad (10)$$

If one assumes a single ion species, (10) reduces to the ideal MHD equations. The different ion species may have different velocities and the first term in Equation 10 (i.e., $(\vec{v}_i - \sum_i \frac{n_i}{n_e}\vec{v}_i) \times \vec{B}$), assumed to be zero in MHD, is in fact nonzero and contributes to the different dynamics identified between the different ion species below.

[13] For the results presented in this paper, the multifluid model assumes three ion populations - a hydrogen solar wind, ionospheric H^+ and ionospheric O_2^+. O_2^+ is used in these simulations to represent heavy ions. Ionospheric hydrogen is included to investigate the difference between light and heavy ions of planetary origin. Viking 1 measured the O_2^+ density at 300 km to be 200–400 cm^{-3} [*Hanson et al.*, 1977]. The inner boundary in the simulations is defined as 250 km above the surface with the number densities of 200 O_2^+ cm^{-3} and 50 H^+ cm^{-3} at the equator. Higher densities at the inner boundary generated unrealistic outflows as the model does not include all possible loss mechanisms such as those due to ion-neutral interactions. The equatorial number densities are reduced gradually with latitude, with the polar number densities 75% of the equatorial number densities, in order to account for variations in ionospheric densities associated with changes in ionization as a function of solar zenith angle. The temperature at the inner boundary is set to 0.5 eV. The number densities and temperature are held fixed at the inner boundary during the simulations. The solar wind density is set equal to 2 ions cm^{-3}. The simulations were initialized assuming a solar wind with a bulk speed of 600 km s^{-1}. Just prior to the formation of the flux ropes analyzed in this paper, the speed was increased to 800 km s^{-1} in order to determine the response by the magnetosphere to a pressure pulse in the solar wind. As it is easier to determine cause and effect in the simulations when only a single parameter is varied, only the solar wind speed was varied to represent disturbed solar wind conditions. Conditions more representative of a solar storm would involve changes in all three solar wind parameters (i.e., density, speed and IMF direction).

[14] The coordinates are such that $\vec{x}$ is in the same direction as the solar wind bulk velocity $\vec{z}$ is perpendicular to the ecliptic plane and pointing north, and $\vec{y}$ is in the ecliptic plane but perpendicular to the solar wind velocity. Thus the positive directions for x and y are opposite that in MSO coordinates, while the z direction is the same as in MSO coordinates. The resolution of the grid varies from 0.4 R_M far from the planet to 42 km around the region of strong magnetic anomalies. The simulation area ranges from 7.9 R_M upstream, to 35.6 R_M downstream, and ±17.4 R_M on the flanks and over the poles. The highest resolution is contained within a region from 0.84 R_M to 1.88 R_M along x, −0.82 R_M to 0.92 R_M along y, and ±0.74 R_M along z. It is surrounded by a region with resolution of 84 km extending from 0.39 R_M to 2.46 R_M along x, −1.49 R_M to 1.98 R_M along y, and ±1.49 R_M along z.

[15] The IMF was assumed to be 2 nT, in the $-B_z$ direction for the run. While various measurements of solar wind parameters by Phobos 2 and MGS show the direction in the ecliptic plane primarily in the B_y direction [cf. *Kallio et al.*, 1995; *Vignes et al.*, 2000], a component of the IMF out of the ecliptic plane represents more disturbed solar wind conditions. Also previous simulations [e.g., *Harnett and Winglee*, 2007] have indicated that the B_z component of the IMF, particularly when in the $-B_z$ direction, will interact most strongly with the anomalous magnetic field. For modeling reason, assuming only a single component for the IMF makes implementing the high-resolution gridding in the tail much simpler. As the model uses a Cartesian grid system, it is difficult to implement the high-resolution gridding if the large-scale current sheet (the region in which flux ropes will typically initiate) is not aligned with either the equatorial plane or noon-midnight meridian.

[16] The model of the Martian magnetic field was provided by *Cain et al.* [2003]. A 90 term internal potential function was generated using 110,000 3-component observations from MGS. For the results presented in this paper, the equatorial plane of Mars was aligned with the ecliptic plane and 180° longitude was oriented along the midnight meridian. The surface magnetic field was allowed to rotate during the run, but the motion associated with the 24.6 h rotation rate was small with regard to the time scales of the plasma dynamics shown here, which occur on minute time scales.

3. Results

[17] Figure 1 shows the time evolution of a flux rope in the Martian magnetotail. Beside a large-scale pressure enhancement on the dayside associated with the formation of a bow shock and a magnetosheath, small-scale features in the total pressure are also present on the flanks and in the tail, associated with the flux rope and the magnetic anomalies. The average stand-off distances of the bow shock and MPB during the simulations, as determined from enhancements in the current density that occur at each boundary (not shown) are 1.68 R_M and 1.37 R_M, respectively. When the solar wind

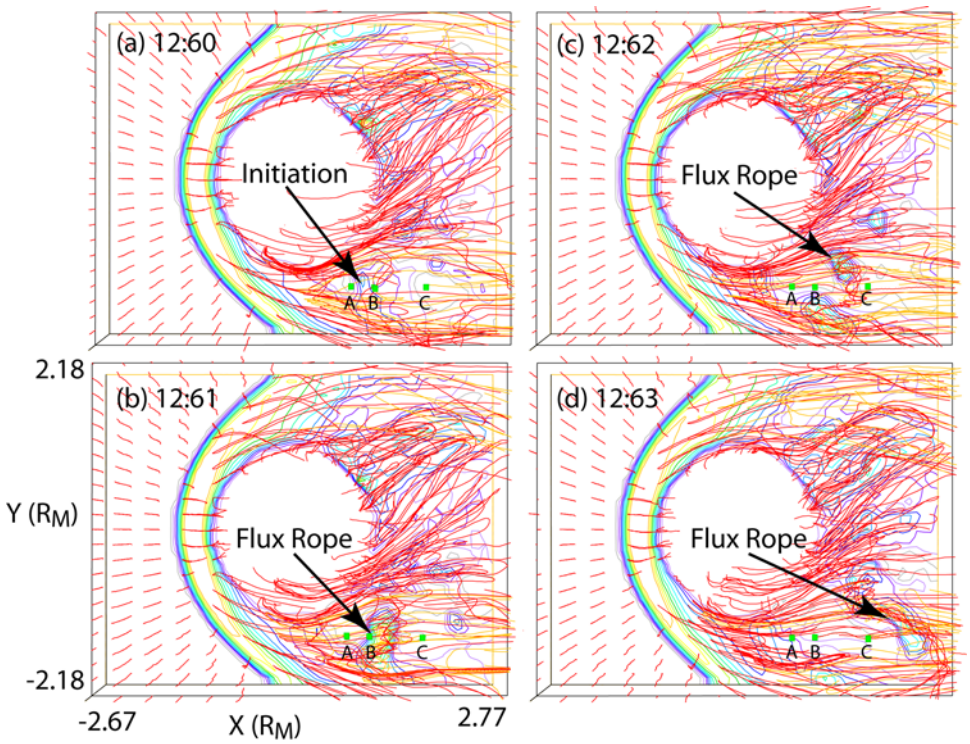

Figure 1. The evolution of a flux rope as viewed from above the north pole. The red and orange lines are magnetic field lines, and the color contours indicate total pressure in the equatorial plane. Orange field lines are ones in which both footpoints of the field line end of the back wall of the simulation area. All other field lines are red. The frames are from Animation S1, showing flux rope 1, but rotated 45°. The green squares indicate positions at which plasma parameters were sampled to generate Figures 2 and 3.

speed increases the stand-off distances move in slightly before returning to approximately their original values. The value for the bow shock stand off distance is within one sigma of the average value determined by *Vignes et al.* [2000], while the stand off distance for the MPB is two sigma from the average value. This discrepancy may indicate that the value assumed for the ionospheric density at the inner boundary is slightly too high.

[18] The flux rope in the tail is evident by the presence of both coiled magnetic field lines and a simultaneous enhancement in the pressure (as indicated by the color contours). The region of enhanced pressure demarcates the extent of the flux rope. The flux rope initiates near the dusk terminator and travels tailward (see dynamic content Animation S1 for a movie of the flux rope motion).[1] Flux ropes are frequently observed in the terrestrial magnetotail [e.g., *Slavin et al.*, 2003] and at the terrestrial magnetopause [e.g., *Russell*, 1989]. The multifluid model has been used to study flux ropes in both locations at the Earth [*Winglee et al.*, 2008a, 2008b]. In both cases, the formation of a thin current sheet is a prerequisite for the generation of flux ropes. The magnetic field lines in Animation S1 indicate the formation of other flux ropes, primarily smaller than the ones shown here (~100 s of km in diameter). The difference between the current simulation and previous simulations of the Martian magnetotail with the multifluid model [e.g., *Harnett and Winglee*, 2006] is that the current version now contains sufficiently high resolution to resolve observed thin current sheets. These results suggest that flux ropes may readily form in thin current sheets within the Martian magnetosphere. For the results shown in Figure 1 and Animation S1, the additional flux ropes form within the cross-tail current sheet region, but also form near closed anomalous magnetic field lines. Investigation of the difference in flux rope formation rate with and without anomalous magnetic field is left for a separate paper.

[19] The flux rope increases in size slightly as it propagates downtail and the magnetic field becomes less tightly wound. Once fully formed, the flux rope is approximately 1200 km in diameter and 2300 km long. It reaches a maximum size of approximately 1700 km in diameter and 2600 km long before it begins to dissipate. The initial length of the flux rope is set by the width of the current sheet at the location the flux rope forms near the dusk terminator. Reconnection occurs across the entire current sheet and the magnetic field tailward of the reconnection point forms the flux rope. The diameter of the flux rope is comparable to the gyroradius of the oxygen ions at the edge of the flux rope. The flux rope is fully formed at an altitude of approximately 2300 km and is at an altitude of 7500 km when it dissipates. It dissipates about 3 min after formation.

[20] Figures 2 and 3 show the evolution of different plasma parameters at three locations that the flux rope passes through. Figure 2 shows the ionospheric hydrogen number density, the z component of the magnetic field, and the x component of the ionospheric ion velocities. The flux rope appears as B_z turning negative, highlighted by the boxes. The B_z component returns to approximately its original value after the flux rope transits past the sampling location,

[1] Animations are available in the HTML.

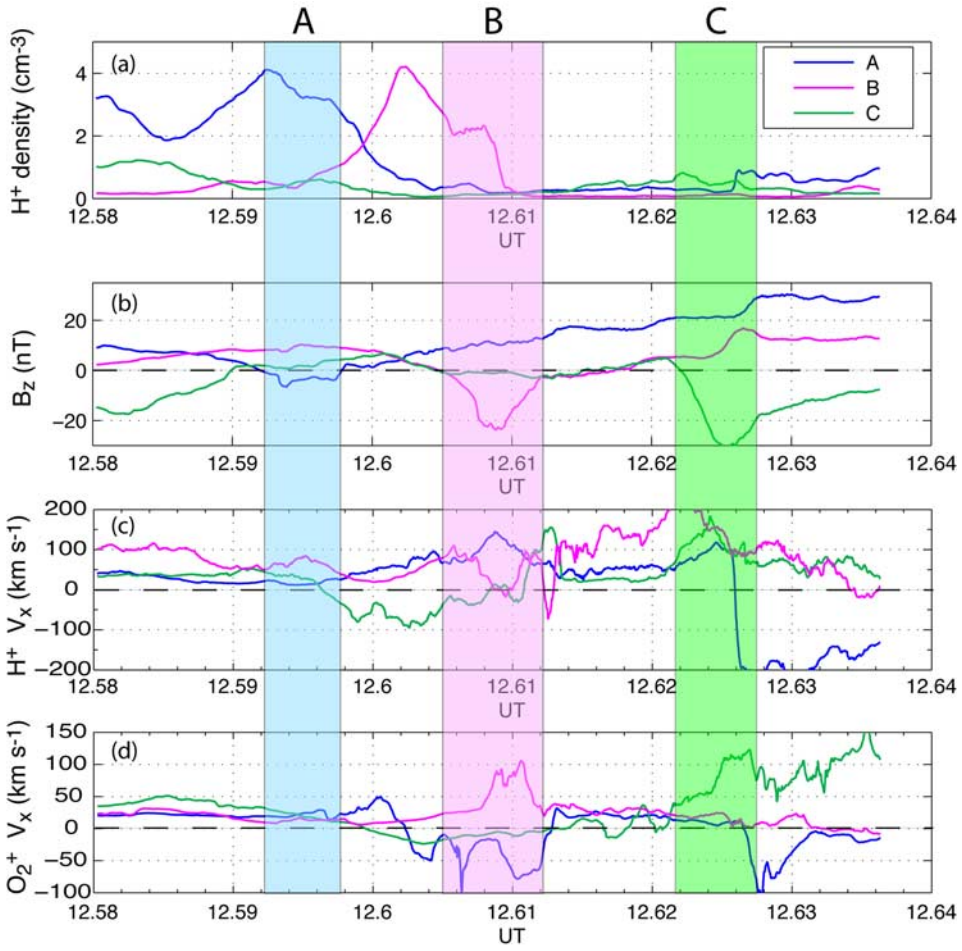

Figure 2. The evolution of (a) the ionospheric hydrogen density, (b) the B_Z component of the magnetic field, (c) the x component of the ionospheric hydrogen velocity, and (d) the x component of the ionospheric oxygen velocity, as measured at three different locations marked in Figure 1. Positive values of v_x are directed tailward. All three positions have a Y and Z position of -1.4 R_M and -0.05 R_M, respectively. The X positions are 0.7 R_M for A, 1.0 R_M for B, and 1.7 R_M for C. The colored boxes show the region of negative B_Z associated with the flux rope passing a given sampling position.

suggesting that continuous reconnection is not occurring. A density enhancement is only associated with the passage of the flux rope for the first two positions, A and B, and in the case of B the strongest enhancement precedes the flux rope slightly. This is due to a snow-plow effect. As the flux rope propagates downtail it sweeps up material in front of it, leading to enhanced densities ahead of the flux rope, in addition to the enhancement inside the flux rope.

[21] Figure 3 shows a hodogram at the three locations. As the axis of the flux rope is primarily aligned along the y coordinate axis when it first forms, the B_x and B_z components are plotted as they are approximately equal to the transverse magnetic components. At position A, the hodogram does not have a strong circular pattern as one would expect for a flux rope. The hodograms for positions B and C show a classical circular pattern associated with flux ropes [e.g., *Cloutier et al.*, 1999]. The combination of the plasma and magnetic field measurements at the three positions indicate that position A is near the initiation point of the flux rope. A density enhancement is present but the flux rope has not fully coalesced and thus the magnetic field is not strongly coiled yet. At position B the flux rope is fully formed, with both a tight winding of the magnetic field into a rope formation and an enhanced density within the core of the flux rope. As the flux rope moves past position C, it is both beginning to dissipate and move across tail (i.e., in the +y direction) as well as down tail (i.e., the +x direction), thus the vector pointing along the core of the flux rope is no longer purely along the y axis and has a component along the x axis. There is no enhancement in density at the position being sampled, primarily because it is on one end of the flux rope, but plasma is also being accelerated out of the core. A density enhancement is still present in the central core of the flux rope. The magnetic field is still tightly wound at position C. As the flux rope continues down tail the magnetic field becomes less tightly wound (Figure 1d) as plasma is accelerated out of the core and the current required to maintain the flux rope cannot be sustained.

[22] Using the time of the most negative value of B_z at each position (Figure 2b), a flux rope propagation speed can be determined. As it is first forming it travels at about 20 km s^{-1} and then increases to a speed to about 40 km s^{-1} before it dissipates. These speeds are about an order of magnitude smaller than flux rope propagation speeds typically

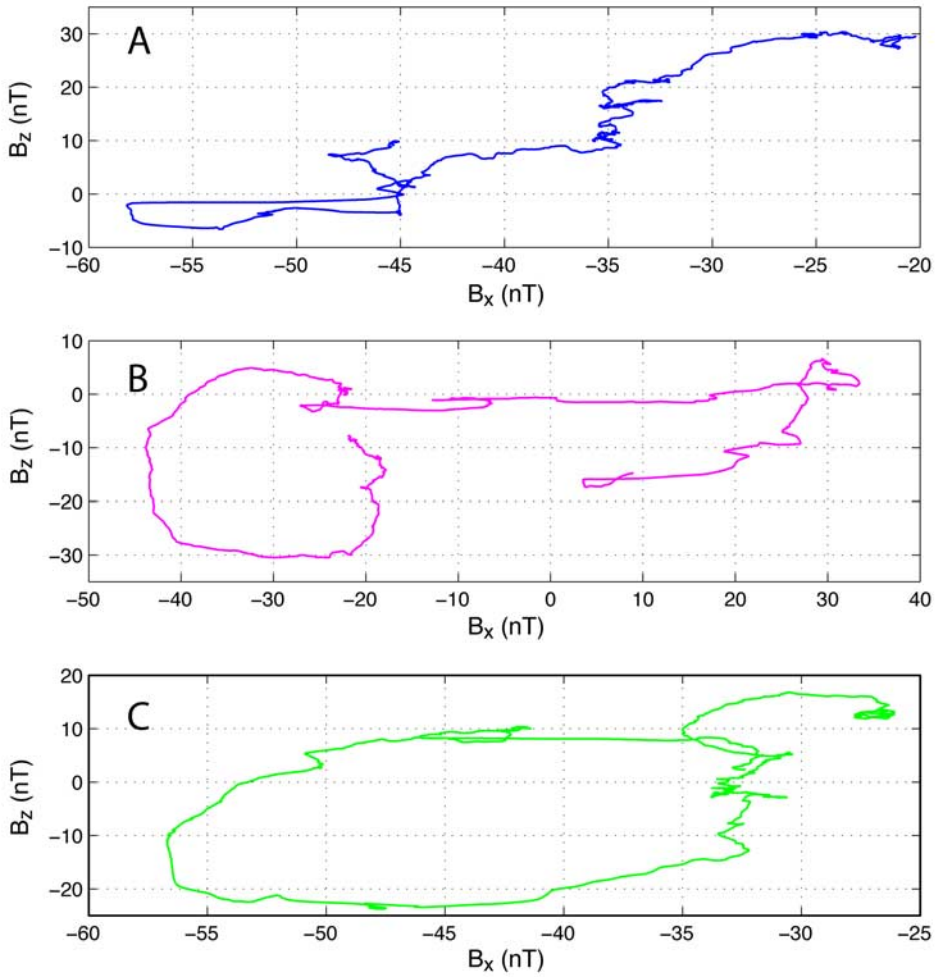

Figure 3. A hodogram of the B_X versus B_Z components of the magnetic field as measured at the three locations marked in Figure 1.

seen at the Earth [e.g., *Slavin et al.*, 2003], but they are comparable to the local Alfven speed just prior to the flux rope transit, which is on the order of 40 km s^{-1}. Typical bulk velocities for plasma in the central tail are on the order of 20–30 km s^{-1}, while the bulk velocities in the neighboring region of the sheath are on the order of 40–60 km s^{-1}. More importantly, the flow speeds of plasma out of the flux rope at the time shown in Figure 4 vary between 100 and 200 km s^{-1} (Figures 2c and 2d). The relative magnitude of these speeds is the reason the flux rope dissipates after only ~2 min. The plasma within the flux rope is accelerated out of the flux rope at speeds approximately an order of magnitude larger than the propagation speed of the flux rope (i.e., the Alfven speed). While it is the electrons that generate the current, the electron number density will be determined by the ion number density as the model assumes quasi-charge neutrality. Thus as ions are accelerated out of the flux rope, the electron density will be reduced as well. Thus the currents necessary for maintaining the flux rope cannot be sustained if the plasma within the flux rope is accelerated out of the flux rope. The current decreases and the flux rope dissipates.

[23] Figure 4 shows ionospheric densities and temperatures, and magnetic field lines in the Martian magnetotail, in a plane parallel to the equatorial plane, but cut through the center of the flux rope shown in Figure 1. Figure 4 shows the flux rope at 1262. It is approximately 1250 km in diameter and 2550 km long at this time. The most prominent feature in the plots of ionospheric densities (Figures 4a and 4b) are the high-density regions on the dawn (right hand) side. This is the tail plasma sheet. Note that the temperature of the plasma sheet is only on the order of 10 eV. Even in the central current sheet, which is below the plane shown in Figure 4, plasma temperatures are only on the order of 10 s of eV. The hottest regions in the tail are in the vicinity of the flux rope, which are on the order of 100 s of eV.

[24] The composition of the plasma sheet is primarily oxygen ions, with the number density of solar wind ions one to two orders of magnitude smaller than the ionospheric ion densities. In the vicinity of the flux rope the composition changes. Within the flux rope the ionospheric ion density is ~20 times the solar wind ion density, while sunward and tailward of the flux rope, the solar wind is the dominate ion species.

[25] The flux rope has a core magnetic field on the order of 100 nT at the time shown in Figure 4, which is 4 times larger than the magnetic field magnitude in the surrounding tail. As the flux rope travels downtail, the current decreases,

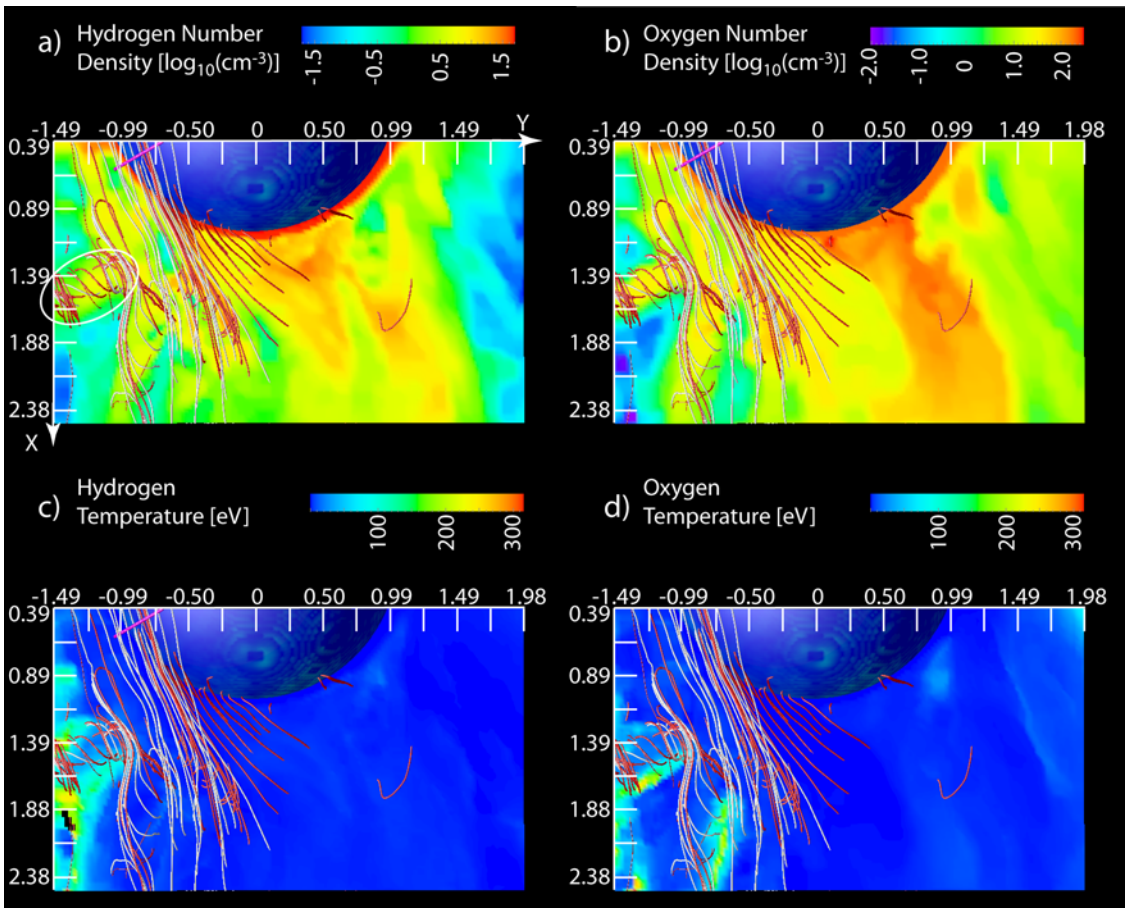

Figure 4. The (a) ionospheric hydrogen density, (b) oxygen density, (c) ionospheric hydrogen temperature, and (d) oxygen temperature in a plane parallel to the ecliptic, as viewed from above the north pole. The red and white lines are magnetic field lines. The different field line colors are for clarity only. The flux rope is circled with a white oval in Figure 4a. Units on the axes are in R_M.

the flux rope becomes less tightly wound and the core magnetic field decreases. Also associated with the flux rope is a significant Hall current. The simulations also indicate an important characteristic of the magnetic field geometry to consider when interpreting data. The magnetic field lines that are not associated with the flux rope show significant dawn-dusk twisting, thus field lines located at midnight in the equator, 1–2 R_M from the surface, actually connect to a premidnight region at the planet. This indicates potentially large errors (~20° longitude) associated with simply mapping the typical magnetic field geometry at 400 km radially outward to higher altitudes.

[26] While flux rope formation has been identified as occurring on the dayside of Mars [*Cloutier et al.*, 1999; *Vignes et al.*, 2000], it has not been officially identified on the night side. To predict what a satellite would observe while transiting though this flux rope, synthetic spectrograms can be generated. The spectrograms are generated by assuming a Maxwellian distribution centered about the bulk speed of a particular species at each given location. The width of the Maxwellian is determined by the temperature of the species at that particular location.

[27] Figure 5 shows the spectrogram for a trajectory traveling through the tailward edge of the flux rope. For comparison with the spectrogram of *Lundin et al.* [2006a], the trajectory begins in the southern hemisphere. The trajectory samples at 2120 local time. It was noted by *Lundin et al.* [2006b] that most observations of inverted-Vs occurred between a local time of 2200 and midnight. The sample trajectory is above a geographic longitude of approximately 140°E. *Lundin et al.* [2006b] indicate that multiple inverted-Vs were observed over approximately the same geographic longitude, near the equator.

[28] The synthetic spectrograms have an inverted-V shape. The peak ion energies are on the order of a keV while the peak electron energies approach a keV. This is similar to the energy range seen by MEX. The inverted-V feature spans a latitude range of approximately 20°. The inverted-Vs shown by *Lundin et al.* [2006b] span latitudes of 10° to 25°. They are observed at altitudes of less than 1000 km to in excess of 8000 km. The flux rope in Figure 5 transits through this altitude range. Note that the highest temperatures are on the leading edge of the flux rope (Figure 5f). This is due to a combination of the snow-plow effect that is evident in Figure 2 and the fast flows emanating from the flux rope. The electric fields generating the fast flows out of the flux rope are at the edge of the flux rope, and will lead to the formation of an energetic region in front of the flux rope. Additionally as both the flux rope and the fast flows propagate downtail, they encounter plasma that has a smaller

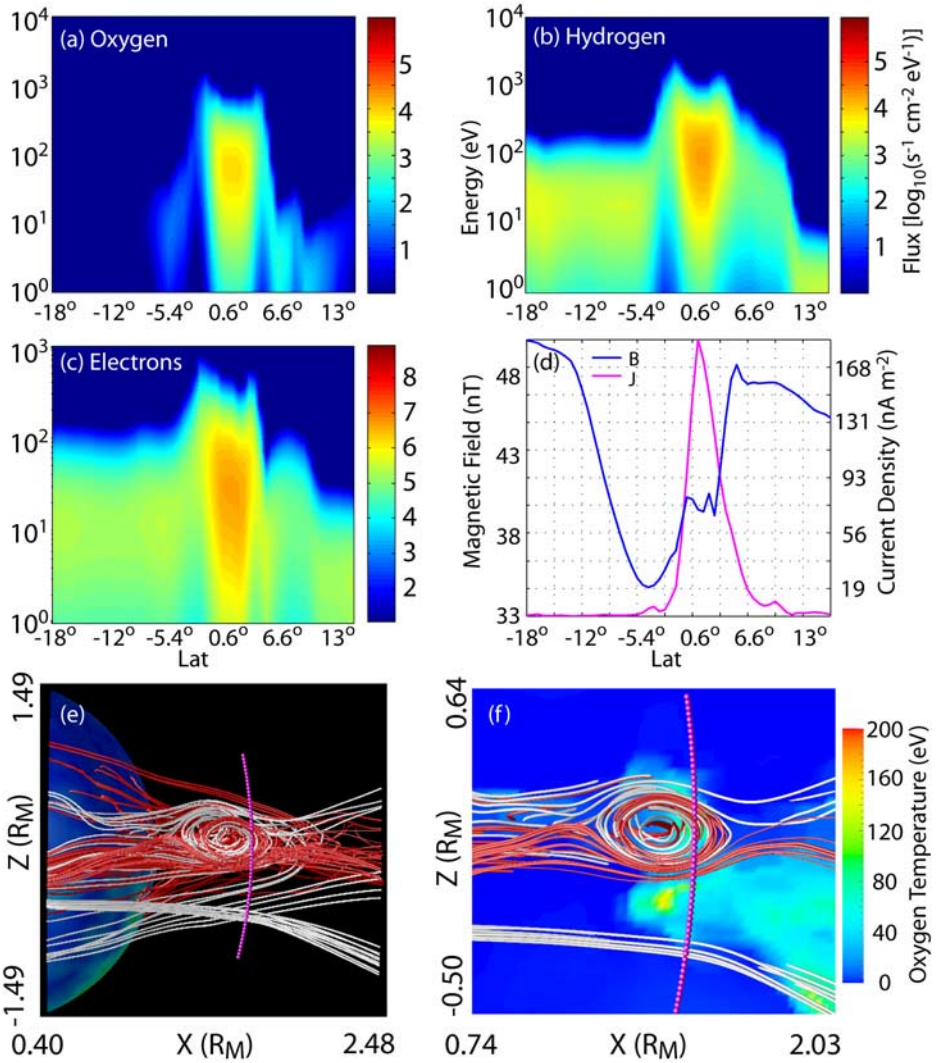

Figure 5. Case 1. Figures 5a–5c are synthetic spectra for oxygen, ionospheric hydrogen, and electrons, sampled along the curve in Figures 5e and 5f. Figure 5d shows magnetic field magnitude (B) and current density (J) data, also sampled along the curve in Figures 5e and 5f. The red and white lines in Figures 5e and 5f are the magnetic field lines as viewed from the dusk terminator. Figure 5e also shows the anomalous magnetic field magnitude at an altitude of 300 km. In addition to the magnetic field geometry, Figure 5f shows the oxygen temperature in a plane cutting through the center of the flux rope. The trajectory is along a constant altitude of 4000 km, and samples at 2120 local time over a geographic longitude of approximately 140°E.

velocity. This sweeps up the ambient plasma (creating the afore mentioned density enhancements), heating it in the process. As a result, the most prominent inverted-V type signatures (i.e., spectra with the highest peak energies along the trajectory) occur when a synthetic satellite trajectory is taken through the edge of the flux rope, not the center.

[29] One difference though between the model spectra and observations is time scale. The inverted-V reported by *Lundin et al.* [2006a] was present over 30 min, much longer than the time scale over which the flux rope in Figure 5 is present. But the two additional cases detailed by *Lundin et al.* [2006b] show enhancements in the electron flux that have structures on the minute time scale and 100s of km spatial scale. One occurs at an altitude of less than 1000 km and the other occurs at an altitude in excess of 8000 km. Also, inverted-V observations that have both a long time and spatial scale may be sampling multiple flux ropes. J. P. Eastwood et al. (private communication, 2008) found evidence for a chain of magnetic islands at Mars, and thus possibly a chain of flux ropes. In the simulations, a second flux rope (Case 2) is initiated at the edge of the flux rope in Figure 4 (Case 1) as it propagates through the tail.

[30] The flux rope that forms in Case 2 appears at 1265 at an altitude of 3570 km (Figure 6a and Animation S1). This one does not propagate downtail like the flux rope shown in Figure 4. It changes in shape but stays at a relatively constant location for several minutes. The Alfven speeds in the region are similar to those around the flux rope in Case 1, but the bulk velocities within the flux rope are 3–4 times smaller than in Case 1. This is due to a combination of two factors.

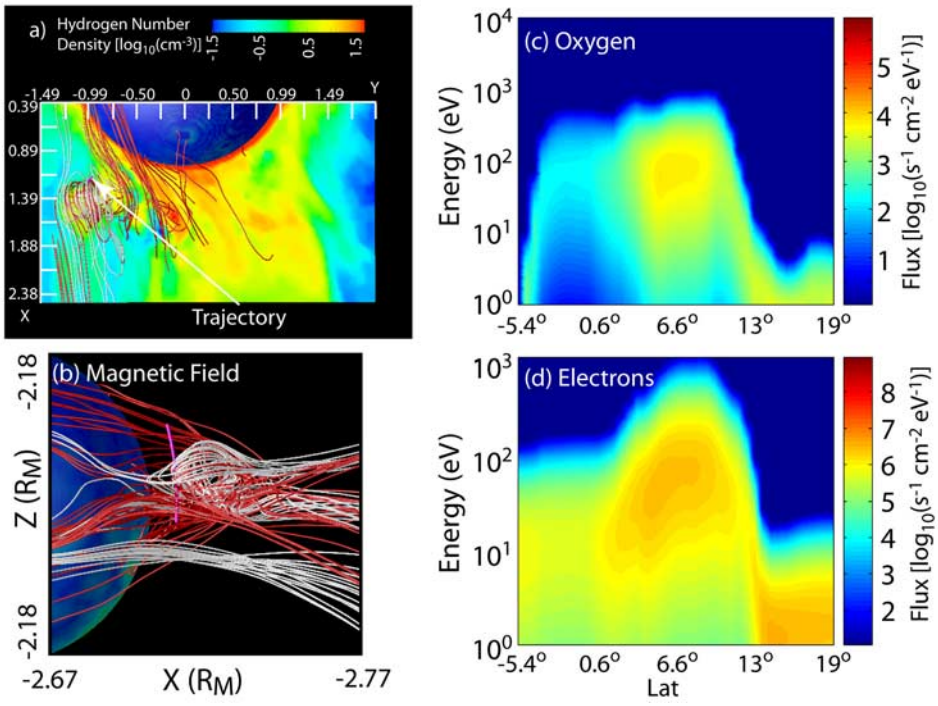

Figure 6. Case 2. Another flux rope forms as the flux rope shown in Figure 4 (Case 1) propagates downtail. Figure 6a shows the hydrogen number density and magnetic field lines, and is in the same form as Figure 4a. Figure 6b shows the magnetic field lines and synthetic satellite trajectory from the dusk terminator and is of the same form as Figure 5e. The trajectory in this case is at a constant altitude of 1.6 R_M (5435 km) at a local time of 2124. Figures 6c and 6d show the oxygen and electron spectra along the trajectory shown in Figure 6b and are of the same form as Figures 5a and 5c.

The flux rope is less tightly wound, and therefore the core magnetic field is only on the order of 50 nT, or only 2 times larger than the ambient magnetic field. Additionally the plasma densities inside the flux rope are ~2 times less than inside the previous flux rope. While the density within the flux rope is dominated by ionospheric oxygen (similar to Case 1), the ratio of ionospheric ion density to solar wind density to smaller than in Case 1 by about a factor of 2 owing to the reduced total density in Case 2.

[31] The reduced ion density leads to a lower electron density and smaller currents surrounding the flux rope as there is less plasma to carry the currents. The magnitude of the current density within the flux rope is approximately half of the previous case. As both the current and the magnetic field are weaker, the Hall currents in this flux rope are approximately half that compared to Case 1, thus the electric fields at the edge of the flux rope 2 are about half of the electric fields in Case 1. This leads to flow speeds at the edge of the flux rope peak around 50–100 km s^{-1}. Therefore the plasma is not accelerated out of the flux rope as quickly, leading to the longer lifetime.

[32] At the time shown in Figure 6, the flux rope has a diameter of approximately 1700 km. An inverted-V shape is present over approximately 20° in latitude. The inverted-V is produced from a trajectory that is at approximately the same longitude as the previous case, and thus over approximately the same geographic region. The peak energies seen in spectra for this flux rope (Figures 6c and 6d) are again similar to those observed by MEX. The peak and mean electron energies are slightly higher in this case than in Case 1, while the peak and mean hydrogen energies are ~5–10 times lower in Case 2. As in Case 1, the highest temperatures occur at the outer edges of the flux rope, thus the most prominent inverted-V signature comes when the simulation results are sampled along a trajectory that skirts the edge of the flux rope.

[33] *Lundin et al.* [2006b] also determined that when inverted-Vs where observed, the electrons appeared to be streaming toward the planet while heavy ions were appeared to be streaming away from the planet. This would produce a current radially away from the planet. Figure 7 shows the components of the current along the trajectories shown in Figures 5 and 6. For both cases, the inverted Vs in the model results are coincident with currents that have a significant component that is pointing radially away from the planet. Figure 7 shows that sampling along certain trajectories can produce a current signature similar to what would be expected for a field-aligned current if one assumes the magnetic field is mostly radial. In these two cases, this is primarily due to the alignment of the flux rope. The current density is highest in the center of the flux rope, and points along the core of the flux rope. In both cases, the core of the flux rope is aligned primarily along a radial vector at the time in which the simulation results were sampled (see Figures 4a and 6a). Following a trajectory that skims the edge of the flux rope samples a region with both elevated current density (which for these orientations is primarily radial) and enhanced plasma temperatures. A trajectory closer to the core of the flux rope would yield higher current densities, but lower peak energies in the spectra. Thus the simulations were sampled at

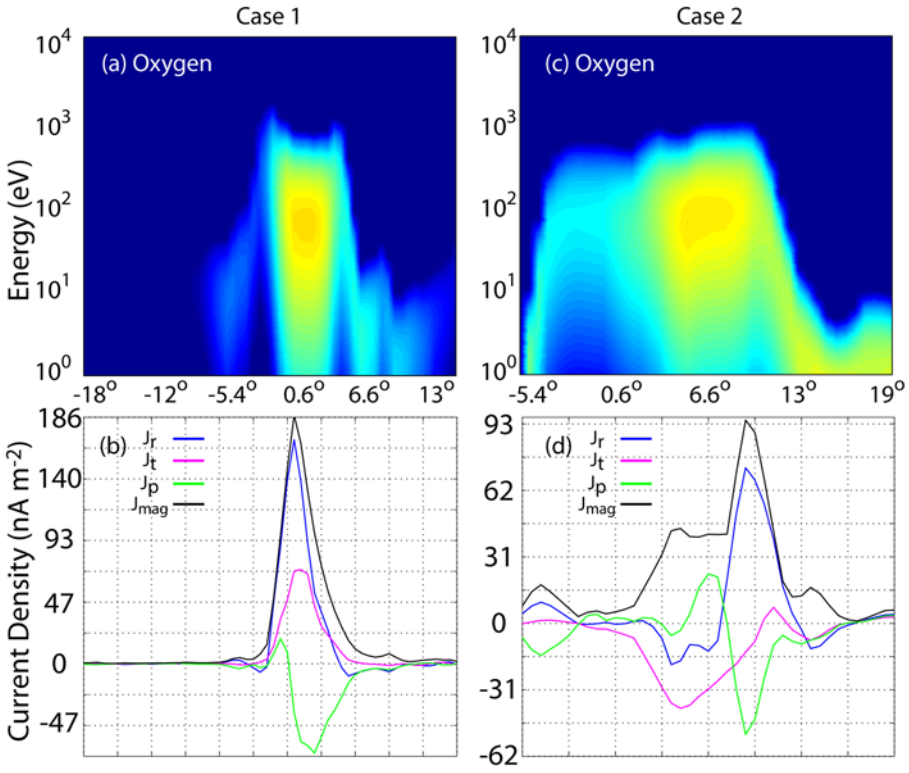

Figure 7. The oxygen spectra and components of the current density for two previous flux ropes discussed. Figure 7a is identical to Figure 5a, and Figure 7c is identical to Figure 6a. Figures 7b and 7d show the corresponding magnitude of the current density (J_{mag}), the radial component of the current density (J_r), the theta component (J_t), and the phi component (J_p).

a time and location to best show that depending on the orientation of the flux rope, the view from a satellite trajectory can be ambiguous.

[34] The flux rope that propagates downtail (Case 1, Figures 1–5) initiates from a region near the dusk terminator (Figure 1a). Figure 8 shows the magnetic field line geometry for the same time as in Figure 4 and is about a minute after initiation. The magnetic field geometry indicates that the flux rope forms as the result of a reconnection event. Reconnection was observed by MGS at an altitude of 400 km on multiple occasions [*Eastwood et al.*, 2008], including one observation that transited across multiple reconnection regions (J. P. Eastwood et al., private communication, 2008). The reconnection region in the simulations forms at an altitude of approximately 700 km and initiates as the increase in the solar wind speed propagated past the planet. The magnetic field geometry prior to reconnection is such that a thin current sheet (~160 km) is present in the region. The increase in solar wind dynamic pressure compresses the magnetosphere and thins the current sheet further, allowing reconnection to occur. Analyzing MGS mapping phase data (at an altitude of 400 km and at 2AM local time), *Halekas et al.* [2006] found thousands of current sheets with thicknesses on the order of 100 km.

[35] Figure 9 is a cartoon of the reconnection and flux rope generation process. The southward IMF drapes around the planet and slides around at the dawn and dusk terminators. A current sheet forms between the alternately directed magnetic field (Figure 9a). The increase in solar wind speed increases the pressure on the magnetosphere, compressing the magnetic field on the flanks, thinning the current sheet. The current sheet becomes thinner than the local cyclotron radius of the dominate ions within the current sheet (in this case oxygen), allowing them to become demagnetized and reconnection to occur just tailward of the dusk terminator. The magnetic field tailward of the reconnection point propagates tailward like a typical draped field line, while the magnetic field sunward of the reconnection point forms the basis of the flux rope (Figure 9b). As the forming flux rope is entrained in plasma flowing tailward, it too is carried downstream, first coalescing then dissipating.

[36] Spectra taken through the reconnection region (Figure 10) also show an inverted-V type structure. Colocated with the region of hot plasma is a current sheet (Figure 10d) with a thickness on the order of 500 km. The peak temperatures are less than in the previous trajectories in the vicinity of the flux rope but the electron spectra in the simulation is comparable to that measured by MGS at reconnection regions. For the case shown by *Eastwood et al.* [2008], the flux of electrons in the 10–100 eV energy range increases by an order of magnitude as MGS passed through the reconnection region, with the largest enhancements in the 30 eV and 60 eV channels. The simulations show enhanced flux between 1 and 100 eV, with the peak enhancement around 10 eV (Figure 10a). The magnetic field magnitude decreased by a factor or 3–4 as MGS transited through the reconnection region with a reversal of the x component of the magnetic field. In the simulation results

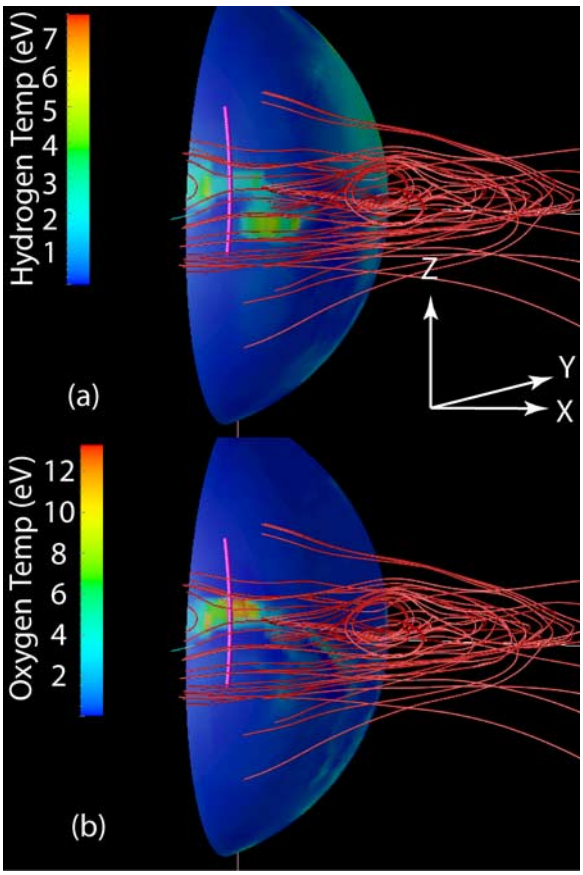

Figure 8. The flux rope initiation region in Case 1 as viewed from above the dusk terminator. The surfaces are at a constant altitude of 700 km. The curve indicates the trajectory along which results are sampled in order to generate the spectra in Figure 10. Both Figure 8a and Figure 8b show the magnetic field lines. Figure 8a shows the hydrogen temperature at 700 km, and Figure 8b shows the oxygen temperature.

the magnetic field similarly undergoes a reversal in the x component of the magnetic field (not shown), while the magnetic field magnitude decreases by a factor of five (Figure 10d).

[37] While the simulation results are similar to MGS observations, the energies of the model electron spectra are lower by a factor of 5 to 10 than the typical energies of auroral type electron spectra thought to be generated through reconnection [*Brain et al.*, 2006]. This may be due to the fact that the simulations ignore wave-particle interactions. This type of interaction can produce significant acceleration and is known to play an important role in acceleration in the auroral regions at the Earth [e.g., *Mozer et al.*, 1980] and may occur in reconnection regions as well [e.g., *Oieroset et al.*, 2002]. Similar processes may occur at Mars, especially if the auroral type electron spectra are in fact related to the reconnection events, as *Eastwood et al.* [2008] show a significant increase in wave power in the vicinity of the reconnection region.

[38] Inverted-Vs are not found exclusively at flux ropes in the simulation results. They can be found along trajectories that cross the cross-tail current sheet, but more importantly, they are also found near the planet in the vicinity of open-closed field line boundaries. Figure 11 shows the oxygen temperature at a constant altitude as viewed from the dawn terminator and the magnetic field geometry near the hot region (similar to Figure 8b). Figure 12 shows the spectra and current along the trajectory through the hot oxygen region shown in Figure 11. Both and inverted-V structure and a significant radial current are present near the open-closed field line boundary. The peak energies for the ions are considerably lower than in the inverted-Vs near the flux ropes (Figure 7), but comparable to the near the reconnection region (Figure 10). The feature is more long-lived than the flux rope, remaining in quasi-equilibrium over the time interval that the flux rope in Case 1 forms, transits downtail, and dissipates, and the flux rope in Case 2 forms. Both the Hall and pressure gradient currents are nonnegligible along the whole region in which the magnetic field lines area shown, with the Hall current comparable in magnitude to the Hall

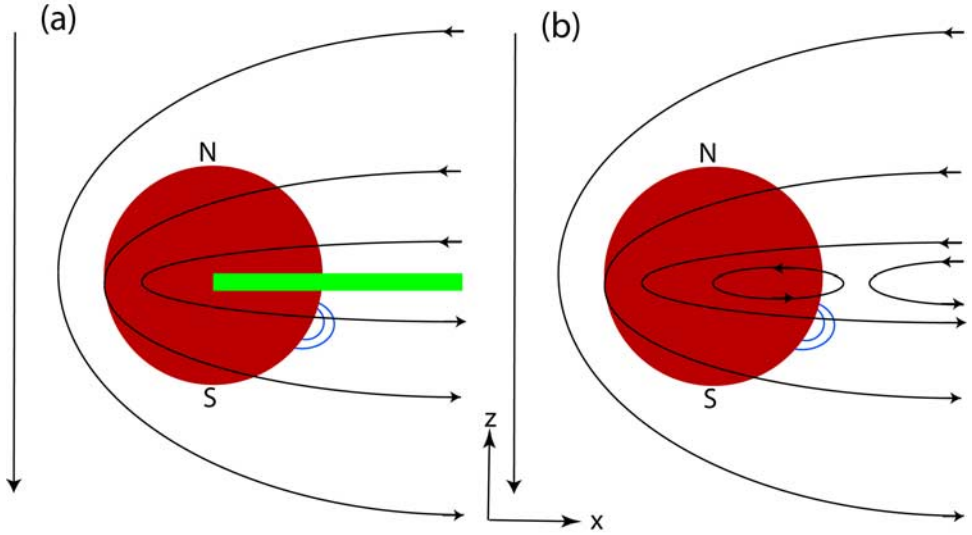

Figure 9. A cartoon of the magnetic field geometry after the reconnection that generates the flux rope. The black lines indicate the IMF. The red disk is Mars (N, north pole; S, south pole), and the blue lines indicate the anomalous magnetic field in the southern hemisphere. The green rectangle indicates the current sheet separating the alternately directed magnetic field.

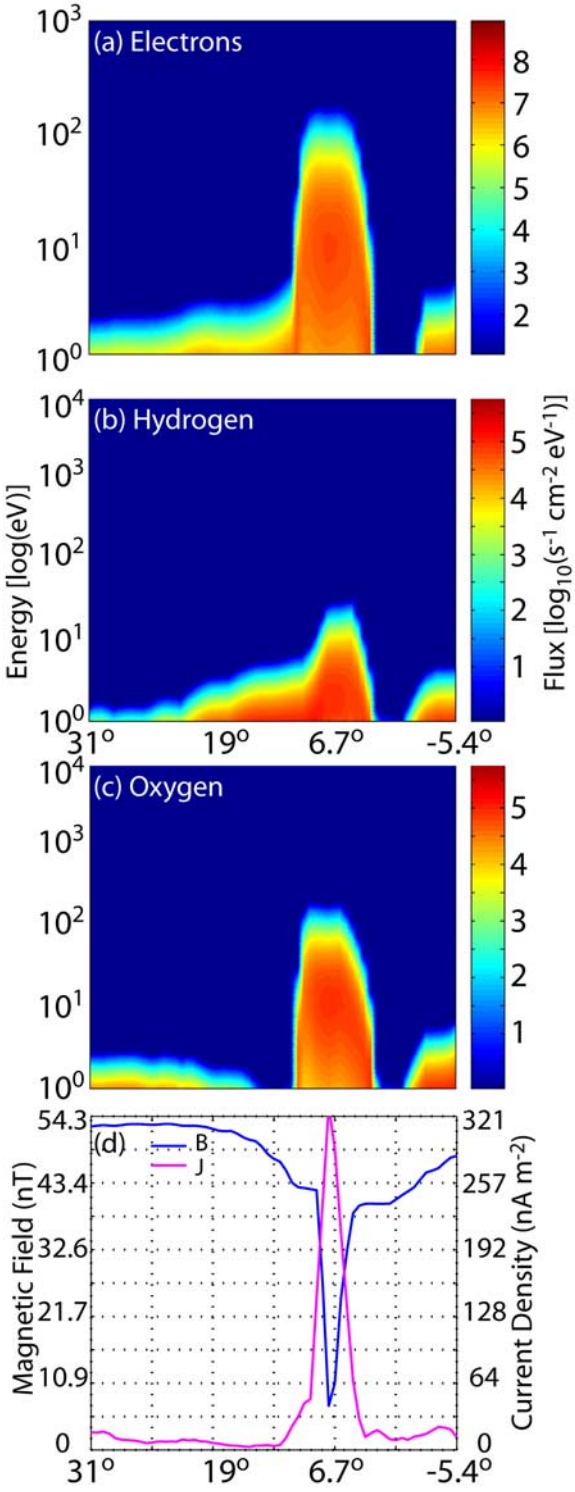

Figure 10. Simulation data sampled along the pink curve in Figure 8. The trajectory begins at 31°N and ends at 5.4°S, along a constant altitude of 700 km, and samples at 2100 local time.

current near the flux rope in Case 1 at 1262 UT. The current associated with the pressure gradient is 1–2 orders of magnitude larger at the flux rope in Case 1 though, than near the open-closed field lines. Qualitatively, these types of currents and plasma signatures agree with the model presented by *Lundin et al.* [2006b] [cf. *Lundin et al.*, 2006b, Figure 13] for a dynamo driven current circuit.

[39] Both the multifluid nature of the model and the high resolution of the simulations are key in the development of both the reconnection region and the flux rope development. The resolution of the model is high enough that it can resolve thin current sheets and the fact that the multifluid model includes ion cyclotron effects means it can capture ion demagnetization. At thin current sheets, the weak magnetic field means that the cyclotron radius of the heavy ions becomes larger than the thickness of the current sheet, resulting in ion demagnetization and reconnection.

[40] This also results in an asymmetry in the location of hot hydrogen and hot oxygen at the reconnection region. In Figure 8, the regions of hottest hydrogen are to the periphery of the center of the thin current sheet while the oxygen, with its larger cyclotron radius, exhibits a broader structure. This was seen in previous multifluid simulations of the thin, postplasmoid current sheet at the Earth [*Harnett et al.*, 2006]. The electron pressure peaked at the center of the postplasmoid current sheet while the most energetic protons lie on the flanks. The structure of the oxygen was more diffuse.

[41] The results for Mars are also similar to the Earth simulations with respect to ion energization, in that oxygen is preferentially energized as compared to hydrogen (Figure 10c versus Figure 10b). The peak hydrogen temperature is ~8 eV while the peak oxygen temperature is ~13 eV. This preferential energization of heavy ion species has important implications with regard to atmospheric loss. The thermal escape energy for hydrogen is 2 eV, and 4 eV for O_2^+. The oxygen spectra in Figures 10c and 5a indicate that reconnection, and flux rope formation, occurring within the ionosphere is a mechanism by which ionospheric ions, particularly heavy ions, can be accelerated well above escape velocities and then directed tailward. The loss rate of oxygen calculated in the simulations increases by 30% when the material in the flux rope is lost downtail. For comparison, previous multifluid simulations [*Harnett and Winglee*, 2006] found that either

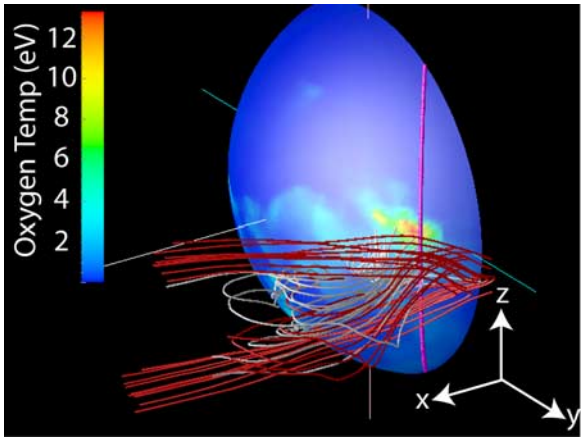

Figure 11. The magnetic field lines and oxygen temperature at 700 km in the vicinity of the dawn terminator at 1262 UT. This is at the same time as the results shown in Figures 4, 5, and 8. The red field lines are primarily open, and the white field lines are primarily closed. The pink curve indicates the trajectory along which results are sampled in order to generate the spectra in Figure 12.

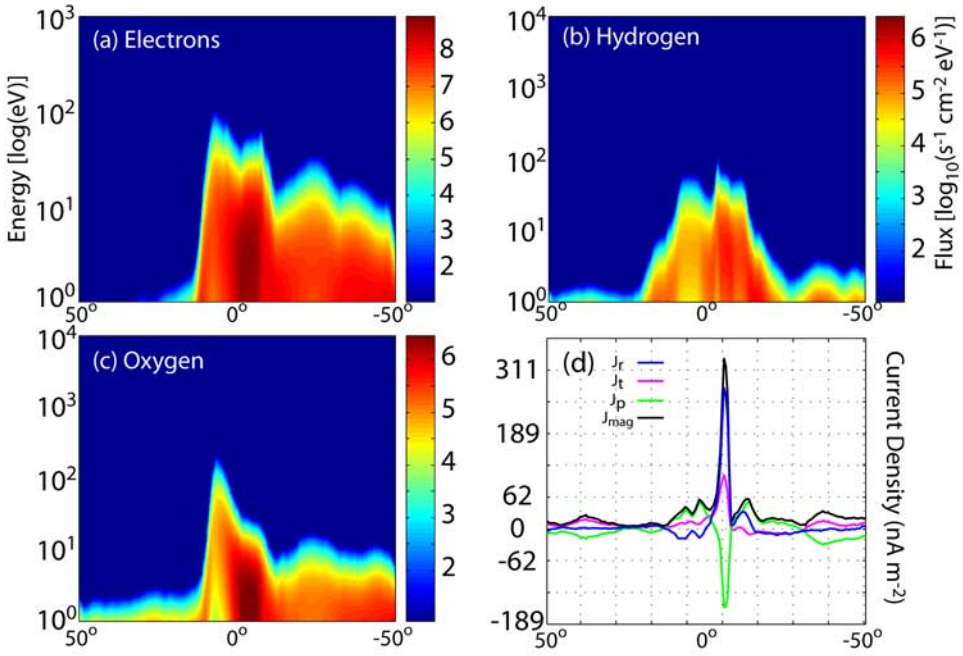

Figure 12. Simulation data sampled along the pink curve in Figure 11. The trajectory begins at 50°N and ends at 50°S, along a constant altitude of 700 km, and samples at 0330 local time, above approximately 240°E geographic longitude.

doubling the speed of the solar wind from 400 km s^{-1} to 800 km s^{-1} or increasing the solar wind density from 2 cm^{-3} to 12 cm^{-3} would approximately double the ionospheric loss rates.

4. Conclusions

[42] High-resolution, 3-D multifluid simulations of the solar wind interaction with Mars suggests flux ropes can form in the Martian magnetotail. Driving the system with a high-speed solar wind can lead to reconnection and the formation of flux ropes with sizes comparable to half a planetary radius. Features key to the formation of reconnection and flux ropes are thin current sheets and ion demagnetization. To capture these in simulations high resolution is necessary so that thin current sheets can be adequately resolved, and ion cyclotron effects must be included to capture ion demagnetization. The length of the flux ropes in the results is comparable to the size of the current sheet in which they form. The diameter of the flux ropes is on the order of the cyclotron radius, at the edge of the flux rope, of the dominate ion species within the flux rope. For the cases shown in this paper, ionospheric oxygen is the dominate ion species.

[43] The comparison of synthetic spectra generated in the vicinity of flux ropes with observations of inverted-Vs by Mars Express indicates that some of the inverted-Vs interpreted as associated with parallel electric fields may actually be due to MEX transiting through either a single flux rope, or a chain of flux ropes. This may be particularly true when the inverted-Vs are observed to have a small spatial or temporal scale, and occur at higher altitudes. The simulations show a significant increase in the radial component of the current density occurs concurrent with inverted-V spectra, also in agreement with observations from MEX. This highlights the difficulty in distinguishing flux ropes from auroral-type structures associated with parallel electric fields using when particle data alone, and in the absence of magnetic field measurements. The results also show another problem associated with the lack of magnetic field measurements, namely the necessity in assuming a model magnetic field at altitude. The simulation results show a significant dawn-dusk twisting in the magnetic field across the tail for southward IMF. This indicates that assuming the magnetic foot point at the satellite location is along only a radial vector toward the planet could lead to significant error ($\sim$20°) in the location of the magnetic foot point, creating misconceptions with regard to which regions of the magnetic anomalies are responsible for modifying the plasma at satellite altitude.

[44] The most unique signature for a flux rope lies in the magnetic field coincident with the inverted-V structure. The presence of a core magnetic field, and a quadrupole signature in the B_z component is used to identify flux ropes in the terrestrial magnetosphere. The flux ropes at Mars posses a core magnetic field 2–4 times larger than the surrounding magnetic field. The quadrupole signature is not strong in the model results though, but this may be due to an inherent differences in the flux ropes at Mars, such as their short lifetimes and smaller-scale size.

[45] The rapid dissipation of one of the flux ropes is different than what is typically seen at Earth. Both observations and simulations indicate the flux ropes at the Earth can travel large distances downtail before they dissipate. The difference at Mars is due to the weak magnetic field. In general, flux ropes propagate at the local Alfven speed. The weak magnetic field strengths at Mars lead to Alfven speeds in the tail that can be at least an order of magnitude smaller than at the Earth. The Hall currents, and electric fields, associated with flux ropes both at the Earth and at Mars will accelerate the

plasma within the flux rope. The crucial difference is that at Mars, the plasma within the flux rope can be accelerated to speeds much larger than the flux rope propagation speed, thus the plasma responsible for generating the currents that sustain the flux rope can be rapidly accelerated out of the flux rope. This will lead to flux ropes with shorter lifetimes and dissipate rapidly as compared to the Earth.

[46] Another important difference between the Earth and Mars is that reconnection occurs much closer to the ionosphere at Mars, indicating a stronger link between the ionosphere and reconnection. This has important implications for the issue of ionospheric loss processes. Reconnection and flux rope formation may play a significant role in driving atmospheric loss, as heavy ions can be preferentially accelerated out of the ionosphere.

[47] **Acknowledgments.** The author would like to thank David Brain and Jasper Halekas for many helpful discussions while analyzing these results. This work was funded by NASA Mars Fundamental grant NNG05GLL9G.

[48] Wolfgang Baumjohann thanks the reviewers for their assistance in evaluating this paper.

References

Acuna, M. H., et al. (1998), Magnetic field and plasma observations at Mars: Initial results of the Mars Global Surveyor mission, *Science*, *279*, 1676–1680, doi:10.1126/science.279.5357.1676.

Acuna, M. H., et al. (1999), Global distribution of crustal magnetization discovered by the Mars Global Surveyor MAG/ER experiment, *Science*, *284*, 790–793, doi:10.1126/science.284.5415.790.

Bertaux, J. L., et al. (2005), Discovery of an aurora on Mars, *Nature*, *435*, 790–794.

Betucci, C., et al. (2005), Structure of the magnetic pileup boundary at Mars and Venus, *J. Geophys. Res.*, *110*, A01209, doi:10.1029/2004JA010592.

Brain, D. A. (2006), Mars Global Surveyor measurements of the Martian solar wind interaction, *Space Sci. Rev.*, *126*, 77–112, doi:10.1007/s11214-006-9122-x.

Brain, D. A., et al. (2005), Variability of the altitude of the Martian sheath, *Geophys. Res. Lett.*, *32*, L18203, doi:10.1029/2005GL023126.

Brain, D. A., et al. (2006), On the origin of aurorae on Mars, *Geophys. Res. Lett.*, *33*, L01201, doi:10.1029/2005GL024782.

Brain, D. A., et al. (2007), Electron pitch angle distributions as indicators of magnetic field topology near Mars, *J. Geophys. Res.*, *112*, A09201, doi:10.1029/2007JA012435.

Brecht, S. (1997), Hybrid simulations of the magnetic topology of Mars, *J. Geophys. Res.*, *102*(A3), 4743–4750.

Cain, J. C., et al. (2003), An n = 90 internal potential function of the Martian crustal magnetic field, *J. Geophys. Res.*, *108*(E2), 5008, doi:10.1029/2000JE001487.

Cloutier, P., et al. (1999), Venus-like interaction of the solar wind with Mars, *Geophys. Res. Lett.*, *26*, 2685–2688.

Crider, D. H., et al. (2002), Observations of the latitude dependence of the location of the Martian magnetic pileup boundary, *Geophys. Res. Lett.*, *29*(8), 1170, doi:10.1029/2001GL013860.

Drake, J. F., et al. (2003), Formation of electron holes and particle energization during magnetic reconnection, *Science*, *299*, 873–877, doi:10.1126/science.1080333.

Eastwood, J. P., et al. (2008), Evidence for collisionless magnetic reconnection at Mars, *Geophys. Res. Lett.*, *35*, L02106, doi:10.1029/2007GL032289.

Halekas, J. S., et al. (2006), Current sheets at low altitudes in the Martian magnetotail, *Geophys. Res. Lett.*, *33*, L13101, doi:10.1029/2006GL026229.

Hanson, W. B., et al. (1977), The Martian ionosphere as observed by the Viking retarding potential analyzers, *J. Geophys. Res.*, *82*, 4351–4363.

Harnett, E. M., and R. M. Winglee (2006), Three-dimensional multifluid simulations of ionospheric loss at Mars from nominal solar wind conditions to magnetic cloud events, *J. Geophys. Res.*, *111*, A09213, doi:10.1029/2006JA011724.

Harnett, E. M., and R. M. Winglee (2007), High-resolution multifluid simulations of the plasma environment near the Martian magnetic anomalies, *J. Geophys. Res.*, *112*, A05207, doi:10.1029/2006JA012001.

Harnett, E. M., R. M. Winglee, and P. A. Delamere (2005), Three-dimensional multi-fluid simulations of Plutos magnetosphere: A comparison to 3D hybrid simulations, *Geophys. Res. Lett.*, *32*, L19104, doi:10.1029/2005GL023178.

Harnett, E. M., R. M. Winglee, and C. Paty (2006), Multi-scale/multi-fluid simulations of the post plasmoid current sheet in the terrestrial magnetosphere, *Geophys. Res. Lett.*, *33*, L21110, doi:10.1029/2006GL027376.

Kallio, E., et al. (1995), Oxygen outflow in the Martian magnetotail, *Geophys. Res. Lett.*, *22*, 2449–2452.

Lin, C. S., and R. A. Hoffman (1982), Observations of inverted-V electron precipitation, *Space Sci. Rev.*, *33*, 415–457, doi:10.1007/BF00212420.

Lundin, R., et al. (2006a), Plasma acceleration above Martian magnetic anomalies, *Science*, *311*, 980–983.

Lundin, R., et al. (2006b), Auroral plasma acceleration above Martian magnetic anomalies, *Space Sci. Rev.*, *126*, 333–354, doi:10.1007/s11214-0069086.

Mitchell, D., et al. (2001), Probing Mars crustal magnetic field and ionosphere with the MGS Electron Reflectometer, *J. Geophys. Res.*, *106*, 23,419–23,427.

Mozer, F. S., et al. (1980), Satellite measurements and theories of low altitude auroral particle acceleration, *Space Sci. Rev.*, *27*, 155–213.

Oieroset, M., et al. (2002), Evidence for electron acceleration up to ~300 keV in the magnetic reconnection diffusion region of the Earths magnetotail, *Phys. Rev. Lett.*, *89*, 195001, doi:10.1103/PhysRevLett.89.195001.

Paty, C., and R. Winglee (2006), The role of ion cyclotron motion at Ganymede: Magnetic field morphology and magnetospheric dynamics, *Geophys. Res. Lett.*, *33*, L10106, doi:10.1029/2005GL025273.

Russell, C. T. (1989), The magnetopause, in *Physics of Magnetic Flux Ropes*, *Geophys. Monogr. Ser.*, vol. 58, edited by C. T. Russell, E. R. Priest, and L. C. Lee, pp. 439–453, AGU, Washington, D. C.

Slavin, J. A., et al. (2003), Geotail observations of magnetic flux ropes in the plasma sheet, *J. Geophys. Res.*, *108*(A1), 1015, doi:10.1029/2002JA009557.

Winglee, R. M. (2004), Ion cyclotron and heavy ion effects on reconnection in a global magnetotail, *J. Geophys. Res.*, *109*, A09206, doi:10.1029/2004JA010385.

Winglee, R. M., et al. (2008a), Multiscale/multifluid simulations of flux ropes at the magnetopause within a global magnetospheric model, *J. Geophys. Res.*, *113*, A02209, doi:10.1029/2007JA012653.

Winglee, R. M., et al. (2008b), Model/data comparisons of ionospheric outflow as a function of invariant latitude and magnetic local time, *J. Geophys. Res.*, *113*, A06220, doi:10.1029/2007JA012817.

Vignes, D., et al. (2000), The solar wind interaction with Mars: Locations and shapes of the bow shock and the magnetic pile-up boundary from the observations of the MAG/ER experiment onboard Mars Global Surveyor, *Geophys. Res. Lett.*, *27*, 4952.

E. M. Harnett, Department of Earth and Space Sciences, University of Washington, Box 351310, Seattle, WA 98195-1310, USA. (eharnett@ess.washington.edu)